Available online at www.sciencedirect.com

ScienceDirect

Journal of Catalysis 254 (2008) 272–284

JOURNAL OF CATALYSIS

www.elsevier.com/locate/jcat

Nanostructured Ti–M mixed-metal oxides: Toward a visible light-driven photocatalyst

A. Kubacka [a], M. Fernández-García [a,*], G. Colón [b,*]

[a] Instituto de Catálisis y Petroleoquímica, CSIC, C/Marie Curie s/n, 28049-Madrid, Spain
[b] Instituto de Ciencia de Materiales de Sevilla, Centro Mixto CSIC-Universidad de Sevilla, C/Américo Vespucio, 49, 41092-Sevilla, Spain

Received 29 October 2007; revised 23 December 2007; accepted 2 January 2008

Abstract

In this report we investigate the structure–activity relationship in Ti–M (M = V, Mo, Nb, W) mixed-metal oxides with anatase structure used for the photoelimination of toluene under sunlight-type excitation. These systems were prepared by a microemulsion method, and their physicochemical properties were characterized by a multitechnique approach using X-ray diffraction–Rietveld, photoelectron spectroscopy, and Raman and UV–visible spectroscopy. The preparation method allowed the incorporation of up to around 20 at% of Mo, Nb, and W, whereas a significantly inferior solubility limit, below 5 at% was observed for V. The presence of nonpunctual defects, intimately related to the existence of MO_x clustering, produced electronic mid-gap states involved in charge recombination and appeared to be the most negative factor influencing photoactivity. The maximization of photoactivity occurred for Ti–M samples with the highest doing level, together with a minimum structural disturbance of the anatase-type structure. The physicochemical bases for the photoactivity behavior of the Ti–M samples as function of the M content and, in particular, the presence of partial (for a specific Ti–M series) or global maxima are discussed.

Keywords: Photocatalysis; Binary Ti–M mixed oxides; TiO_2; Anatase; Visible and sunlight absorption and excitation; Pollutant and toluene mineralization and degradation

1. Introduction

Titanium dioxide (TiO_2) is one of the most prominent oxide materials in various industrial applications related to catalysis, including the selective reduction of NO_x in stationary sources [1,2] and photocatalysis for pollutant elimination [3,4] and organic synthesis [5]. TiO_2-anatase is by far the most widely used photocatalysts due to its wide availability, modest cost, and nontoxicity for humans [3,4]. TiO_2-anatase is an *n*-type semiconductor with a wide bandgap (3.0–3.4 eV depending on primary particle size and other properties) [6], which requires UV light to create energy-rich electron–hole pairs on absorption. In optical-related applications, including all those aiming to use solar light as the energy source, it is desirable to exploit lower energy photons, thus extending bandgap excitations into the visible regime. The introduction of doping cations into the TiO_2-anatase structure to lower the optical bandgap energy is the most common method used to reach this goal [3,6]; however, it also seems a delicate matter, because, at the same time, it would be necessary to avoid creation of unwanted charge recombination centers and/or localized electronic states, which would prevent efficient charge separation of excited electron–hole pairs. In addition, uncontrolled lowering of the conduction band may place the band edge below the O_2 affinity level, jeopardizing the formation of oxygen radicals, which are key intermediates in photocatalytic reactions [3,4].

Despite these potential problems, to date the most effective way of approaching a continuous and systematic reduction of the TiO_2-anatase bandgap energy is bringing by doping cations occupying substitutional positions in the network. Theoretical analysis of the substitutional doping showed that the threshold energy of radiation energy absorption decreased proportionally with the number of doping atoms; in fact, for a random distribution of substitutional acceptors/donors of charge, a Gaussian-

---

[*] Corresponding authors.
E-mail addresses: mfg@icp.csic.es (M. Fernández-García), gcolon@icmse.csic.es (G. Colón).

0021-9517/$ – see front matter © 2008 Elsevier Inc. All rights reserved.
doi:10.1016/j.jcat.2008.01.005

type density of states appeared at the upper/lower part of the valence/conduction bands [7]. The corresponding density of states is directly proportional to the number of doping ions, giving thus a powerful tool for managing visible light (sunlight) absorption. The trade-off on visible light absorption between the aforementioned potential negative effects derived from the presence of localized electronic states and/or other recombination centers and the positive influence in the bandgap energy and subsequent enhancement of the visible-light absorption power is a matter of intense research and remains essentially an open question. It can be stressed that such balance is characteristic of sunlight active systems and has no physicochemical analogy with the corresponding balance achieved between positive and negative effects of cation doping on UV-light excitation.

In this paper, we explore the potential of group V/VI elements as visible light photocatalytic materials. Substitutional TiO_2-anatase-based mixed-metal oxides has been successfully synthesized using Ca, Sr, and Ba [8], V [9–13], Fe [14,15], Cr [10], Zr [16,17], Ta [13,18], Nb [13,18,19], Mo [20], W [21–23], and Sn [24,25]. However, only in the cases of Nb, Mo, and W did we expect to fulfill the two aforementioned primary conditions; production of an anatase-type mixed-oxide structure with a high solubility limit (e.g., with a high concentration of doping ions) and a red-shifted bandgap energy with respect to the parent TiO_2-anatase oxide [18–23]. For completeness, we also studied other V/VI group elements, including V and Cr, because these are frequently used as visible light-driven photocatalysts [9–12], although they may not afford the two aforementioned conditions. Nevertheless, in our case, we were not able to obtain a dominant anatase-type structure using Cr as a doping cation; all of the samples prepared exhibited significant quantities of rutile. The remaining cations (Ca, Sr, Ba, Fe, Zr, Ta, and Sn) gave bandgap energies that were blue-shifted or without shifting with respect to the parent TiO_2 oxide, and thus are inadequate for our purposes. Therefore, we synthesize V-, Nb-, Mo-, and W-doped TiO_2-anatase materials using a microemulsion method, which ensures careful control of the morphological (e.g., primary and secondary particle size) and structural (e.g., homogeneity) properties of the resulting solids. Some of the series (i.e., V-, W-) were studied previously [12,21], but here we report new experimental data using a multitechnique approach intended to establish a link between the short-range and long-range structural properties of the solids and their electronic properties. This basic knowledge would allow (vide supra) rationalization of the photochemical activity and behavior. We evaluated photocatalyst performance using the gas-phase elimination of toluene, which is considered an important constituent of anthropogenic emission in urban atmospheres. In addition, it is a very demanding reaction and thus provides a tough test of the potential of the Ti–M (M = V, Nb, Mo, W) systems in the context of photoelimination of organic pollutants.

2. Experimental

Materials were prepared using a microemulsion preparation method through the addition of titanium tetraisopropoxide to an inverse emulsion containing an aqueous solution (0.5 M) of ammonium metavanadate (Aldrich) or molybdate (Aldrich), hydrated niobium nitrate (Sigma), or ammonium tungsten oxide (Aldrich) dispersed in *n*-heptane, using Triton X-100 (Aldrich) as a surfactant and hexanol as a cosurfactant. Water/titanium and water/surfactant molar ratios were 18 and 110, respectively, for all samples. The resulting mixture was stirred for 24 h, centrifuged, decanted, rinsed with methanol, and dried at 298 K for 12 h. Following the microemulsion preparation method, the amorphous Ti–M (M = V, Nb, Mo, W) material was calcined under air for 2 h at 723 K. Samples are named Mn, *n* being the metal atomic content. Reference TiO_2, V_2O_5, Nb_2O_5, MoO_3, and WO_3 oxides also were synthesized using the same procedure. Table 1 shows the main characterization results for the synthesized materials. Ti:M composition was analyzed by using inductively coupled plasma and atomic absorption (ICP-AAS), whereas BET surface areas were measured by nitrogen physisorption (Micromeritics ASAP 2010).

Table 1
Main characteristics of the Ti–M materials

Sample	M atomic percentage (%)[a]	BET surface area ($m^2\,g^{-1}$)	Size (nm)[b]
TiO_2	–	106	13.3
		Ti–V	
V0.6	0.6	65	8.9
V1	1.2	66	8.1
V2.5	2.5	60	8.5
V5	4.9	60	14.0
V8	8.1	48	12.3
V18	18.2	33	13.2
		Ti–Nb	
Nb10	9.7	112	8.8
Nb20	20.2	125	10.8
		Ti–Mo	
Mo8	7.9	130	8.1
Mo12	12.3	144	6.6
Mo26	26.2	77	5.7
		Ti–W	
W2	1.8	116	11.6
W4	3.7	111	12.0
W11	10.9	106	9.4
W14	13.8	108	10.7
W19	19.1	122	7.9
W20	20.4	101	–[c]
W27	27.0	87	–[c]

[a] Cation basis (100 × W/(W+Ti)) by ICP-AAs.
[b] For anatase-type structure using XRD and the Willianson–Hall method.
[c] Not measured with confidence.

Rietveld analysis was carried out using the General Structure Analysis Software package (GSAS). X-ray diffraction (XRD) patterns were recorded in the range $10° < 2\theta < 120°$ at steps of 0.02° steps, using a Siemens D-501 diffractometer with Ni filter and graphite monochromator with a CuK_α X-ray source. Peak shapes were quantified by a pseudo-Voigt function. Background intensities were described by a cosine Fourier series with 10 coefficients. Each structural model was refined to convergence, with the best result selected on the basis of agreement factors and stability of the refinement. In the last cycle of the refinements, all parameters were varied, including scale factor, zero shift, peak shape parameter, half-width, and lattice parameters. The particle sizes, reported in Table 1, were calculated from XRD patterns using the Willianson–Hall method, which takes into account the contributions of strain and particle size to XRD peak broadening [26].

UV–visible transmission experiments were performed with a UV–Vis Varian 2300 apparatus. Band gap analysis for an indirect/direct semiconductor was done following standard procedures, for example, plotting $(h\nu a)^n$ ($n = \frac{1}{2}$ or 2 for indirect or direct semiconductor; $h\nu$ = excitation energy, a = absorption coefficient) versus energy and obtaining the corresponding tangent value for null absorption [6]. Raman data were acquired using a Renishaw dispersive system 1000 equipped with a single monochromator, a holographic Notch filter, and a cooled thermal conductivity detector. Samples were excited using the 514-nm Ar line. XPS data were recorded on 4×4 mm^2 pellets, 0.5 mm thick, prepared by gently pressing the powdered materials that were outgassed in the prechamber of the instrument at 150 °C up to a pressure below 2×10^{-8} Torr to remove chemisorbed water from their surfaces. The Leibold–Heraeus LHS10 spectrometer main chamber, working at a pressure below 2×10^{-9} Torr, was equipped with an EA-200 MCD hemispherical electron analyzer with a dual X-ray source working with AlK_α ($h\nu = 1486.6$ eV) at 120 W and 30 mA. C1s was used as the energy reference (284.6 eV).

Activity and selectivity for the gas-phase photooxidation of toluene were tested in a continuous-flow annular photoreactor (described elsewhere [27]) containing ca. 30 mg of photocatalyst as a thin layer coating on a Pyrex tube. The corresponding amount of catalyst was suspended in 1 mL of water, painted on a Pyrex tube (cutoff, ca. 290 nm), and dried at room temperature. The reacting mixture (100 mL/min) was prepared by injecting toluene (Panreac, spectroscopic grade) into a wet (ca. 75% relative humidity) 20 vol% O_2/N_2 flow before entering the photoreactor at room temperature, yielding an organic inlet concentration of ca. 800 ppmv. Under such conditions, the reaction rate is zero order with respect to the total flow and hydrocarbon/oxygen concentrations. After the mixture was flowed for 1 h (control test) in the dark, the catalyst was irradiated by four fluorescent daylight lamps (6W, Sylvania F6W/D) with a radiation spectrum simulating sunlight (UV content of 3%), positioned symmetrically outside the photoreactor. Reference experiments with UV lamps (Sylvania F6WBLT-65; 6W, maximum at ca. 350 nm) were run using the same reaction setup and procedure. Reaction rates were evaluated (vide supra) under steady-state conditions, typically achieved after 3–4 h from the start of irradiation. No change in activity was detected for all samples within the subsequent 6 h. The concentration of reactants and products was analyzed using an online gas chromatograph (HP G1800C) equipped with an HP5 capillary column (0.25 mm i.d. × 30 m) and a flame ionization detector using a SIM mode.

3. Results

Representative examples of the Ti–M XRD patterns are presented in Fig. 1S of the Supporting information. The plot gives evidence that all samples contained titania, mainly in the anatase-type structure (JPCDS 84-1286) with a crystallinity behaving very differently for the four Ti–M (M = V, Nb, Mo, W) series of samples. As summarized in Table 1, the surface area of the materials was >50 m^2 g^{-1} in most of the samples. As a general trend, crystallite size decreased concomitantly to a surface area (mild) increase as the M content of the Ti–M materials increased for Mo and W up to certain upper limit (ca. 20 at%), was roughly constant (smooth increasing) for Nb, and displayed well-differentiated behaviors above and below 5 at% for V. However, some samples (e.g., W11) did not follow this general trend. The presence of the M heteroatom affected the morphological properties, affording constant, increasing, or decreasing behaviors of the primary particle size and surface area as a function of the nature of the M atom.

For M loadings <20 at%, XRD patterns also showed the presence of a brookite phase (JPCDS 2-514), and for Ti–V samples with a V content >5 at%, of vanadates (see Supporting information, Fig. 1S). The V-only detected XRD peaks can be ascribed to V_4O_9-type (JCPDS 27-1065) or $(V_5O_{14})^{3-}$-type, rossite-like (JCPDS 36-442) structures [12]. The solubility limits for the remaining heteroatom cations are, as expected [18–23], significantly superior and can be roughly estimated from our data to be in the three cases around 20 at%. After this limit, MoO_x (distorted structures related to JCDS 05-0508) and WO_3 (JPCDS 05-0364 and 85-2459) oxides also were detected. These are the MO_x (M = Mo, W) polymorphs obtained during synthesis of the single oxides, indicating the prevalence of the preparation method when driving to these phases. Rietveld analysis of the XRD patterns provided evidence of the more or less constant brookite-to-anatase ratio (10 ± 5%) of all Ti–M materials and gave the cell parameters for the dominant TiO_2-anatase phase (Fig. 1).

Fig. 2 shows the Raman spectra for the Ti–Nb and Ti–Mo series; Fig. 2S in Supporting information gives the corresponding spectra for the Ti–V and Ti–W series. The presence of both minor brookite (weak peaks or shoulders at ca. 245, 320, 365, and 450 cm^{-1} [28]) and dominant anatase (ca. 144, 195, 399, 517, and 639 cm^{-1} [29]) polymorphs in all Ti–M samples was again confirmed using Raman spectroscopy. In good agreement with the XRD study, Raman detected the presence of an additional M–O phase only at a M content <20 at% in the Ti–V series. In the latter case (Fig. 2S), bands at ca. 280, 850–862, 905–910, 935, and ca. 970 (shoulder) cm^{-1} allow definitive ascription to a surface vanadate species with metarossite-type structure [30]. In addition, the absence of Raman frequencies attributable to the presence of M in titania interstitial positions [31] provides further evidence of the formation of Ti–M substitutional mixed-metal oxides. In contrast, the spectra reported in Figs. 2 and 2S enable the analysis and estimation of M atoms at the material surface through detection of M=O and M–O–M related modes [6,32]. A detailed plot of the M-containing active Raman bands is provided in Fig. 3. As is well known, this allows analysis

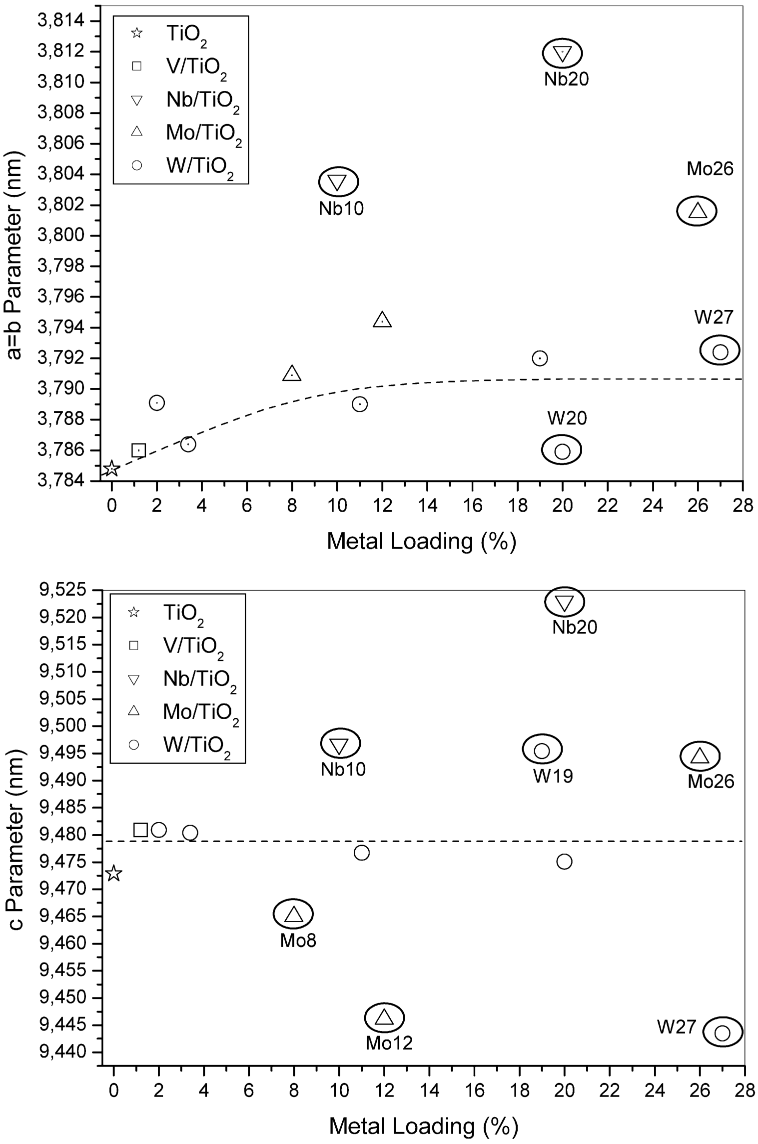

Fig. 1. Anatase cell parameters from XRD–Rietveld analysis. Dashed lines are only a guide for the aids.

of the aggregation state of the M atom at surface (and in certain cases subsurface) layers, differentiating between isolated and oligomeric species, and estimation of their relative abundance [31,32] In brief, the band at ca. 960–975 cm^{-1} (Fig. 3) indicates the presence of isolated surface W species, whereas the presence of small surface aggregates of Mo is demonstrated by the Mo=O (ca. 965 cm^{-1}) and Mo–O–Mo (broad contribution ca. 700–940 cm^{-1}) bands for samples with a content >8 at%. The case of V has been addressed previously, demonstrating the presence of well-developed surface vanadate structures (858, 907, and 936 cm^{-1} in Fig. 3) for an atomic content >ca. 5% [12]. Interestingly, the absence of Nb surface species was noted on Raman (Fig. 3). This will be further analyzed using XPS.

A final point regarding XRD and Raman data concerns the stability of the Ti–M materials under reaction conditions. Postreaction specimens show apparent differences only with respect to the fresh, calcined samples in Raman spectroscopy, giving less-intense peaks (Figs. 2 and 2S). Based on the XRD intensity/width and Raman width invariance, the effect in the intensity of the Raman peaks is likely related to carbonaceous residues accumulated on the surface during reaction.

An XPS study of the samples was devoted to analyzing the chemical state of the cations and surface properties and characteristics. Table 2 summarizes the binding energies of Ti, M, and O ions in selected Ti–M systems. Concerning the oxidation state of the cations [33], the study indicates the exclusive presence of Ti(IV) at 458.5 ± 0.5 eV. The Ti–V series showed, as expected from the XRD/Raman study, the presence of two oxidation states, V(IV) and V(V), with the latter predominant at the surface. The Nb species displayed a 207.0 ± 0.1 eV binding energy, somewhat inferior to the characteristic Nb(V) species in the Nb_2O_5 oxide matrix but well above Nb(IV). This is likely an effect of the coordination change, which may be inferred from the presence of a heteroatom with a larger ionic radius (Nb, 0.64 nm; Ti, 0.605 nm for 6-fold coordina-

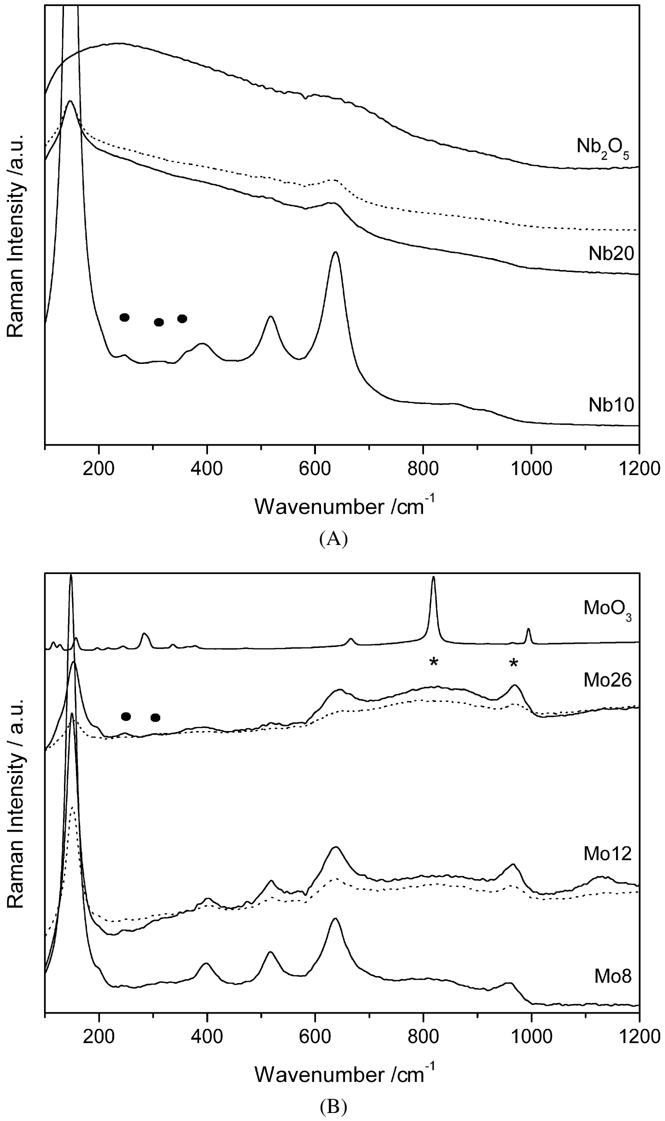

(A)

(B)

Fig. 2. Raman spectra of Ti–M materials: (A) Ti–Nb, and (B) Ti–Mo series of samples. Full line: calcined samples; dotted line: post-reaction samples. Circles and starts highlight, respectively, brookite and MO_x associated bands.

Table 2
Surface M loading and binding energies extracted from XPS data in Ti–M materials

Sample	Surface M loading	Binding energy (eV)					
		Ti (2p3/2)	O (1s)	V ($2p_{3/2}$)	Nb ($3d_{5/2}$)	Mo ($3d_{5/2}$)	W ($4d_{5/2}$)
V1.2	–	458.2	529.4	517.2	–	–	–
V5	~7	458.1	529.5	517.0	–	–	–
V8	~9.9	457.8	529.2	516.5	–	–	–
Nb10	11.1	458.8	530.1	–	207.0	–	–
Nb20	21.9	458.6	530.1	–	206.9	–	–
Mo8	11.6	458.7	530.1	–	–	232.5	–
Mo12	15.4	458.8	530.2	–	–	232.7	–
Mo26	24.5	458.9	530.3	–	–	232.7	–
W2	2.7	458.3	529.7	–	–	–	247.2
W11	13.5	458.7	530.1	–	–	–	247.3
W14	14.1	459.0	530.6	–	–	–	247.5
W19	20.3	459.2	530.5	–	–	–	247.7
W27	25.7	459.1	530.6	–	–	–	247.8

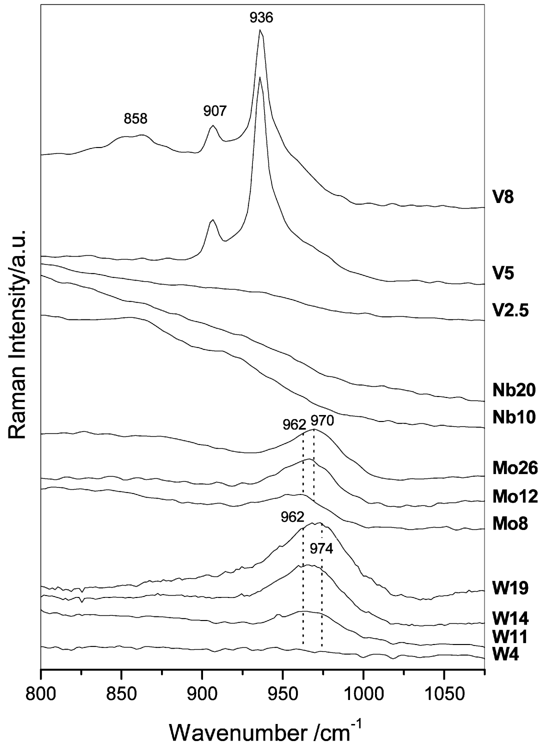

Fig. 3. Detail of Ti–M sample Raman spectra showing bands associated to M-containing species.

tion [34]) at TiO_2-anatase substitutional positions suffering a modest lowering of symmetry and/or local disordering to accommodate a larger cation. Finally, Mo and W binding energies of 232.6 ± 0.1 and 247.5 ± 0.3 eV, respectively, can be ascribed to Mo(VI) and W(VI) oxidation states, although certain Mo(V) fractions could be detected in the Mo system, in all cases $<5\%$. In these cases, there was a practical match of ionic radius between Ti and the heteroatom in the $+6$ chemical state (Mo, 0.59 nm; W, 0.60 nm [34]). The surface M/Ti ratios obtained from the XPS data for the calcined specimens are reported in Table 2. The data provide evidence of a rather limited surface segregation for the Ti–M samples below the corresponding anatase solubility limits. This holds for both the calcined and postreaction (result not shown) samples.

A further point of interest evolving from the XPS study is unveiled by a detailed analysis of the O1s peaks. Fig. 4 displays representative O1s XPS data, and Table 3 summarizes the peak fitting analysis. Essentially, three different contributions were observed in these samples: the first associated with oxygen lattice ions of the anatase network (ca. 530.0–530.5 eV), the second with surface hydroxyls at titania surfaces (ca. 530.9–531.5 eV [35]), and the third with the Ti–Nb series at ca. 533.0 eV. This contribution can be associated with the presence of Nb-rich zones within the TiO_2-anatase structure, because it approached the characteristic binding energy of the single oxide at surface positions [36] and appeared in samples in which absence of Nb-only phases was demonstrated using XRD–Rietveld and the most sensitive Raman spectroscopy (which, under appropriate conditions, may detect 0.1 wt% of a surface V-, Nb-, Mo-, or W-containing phase) [32]. Such a

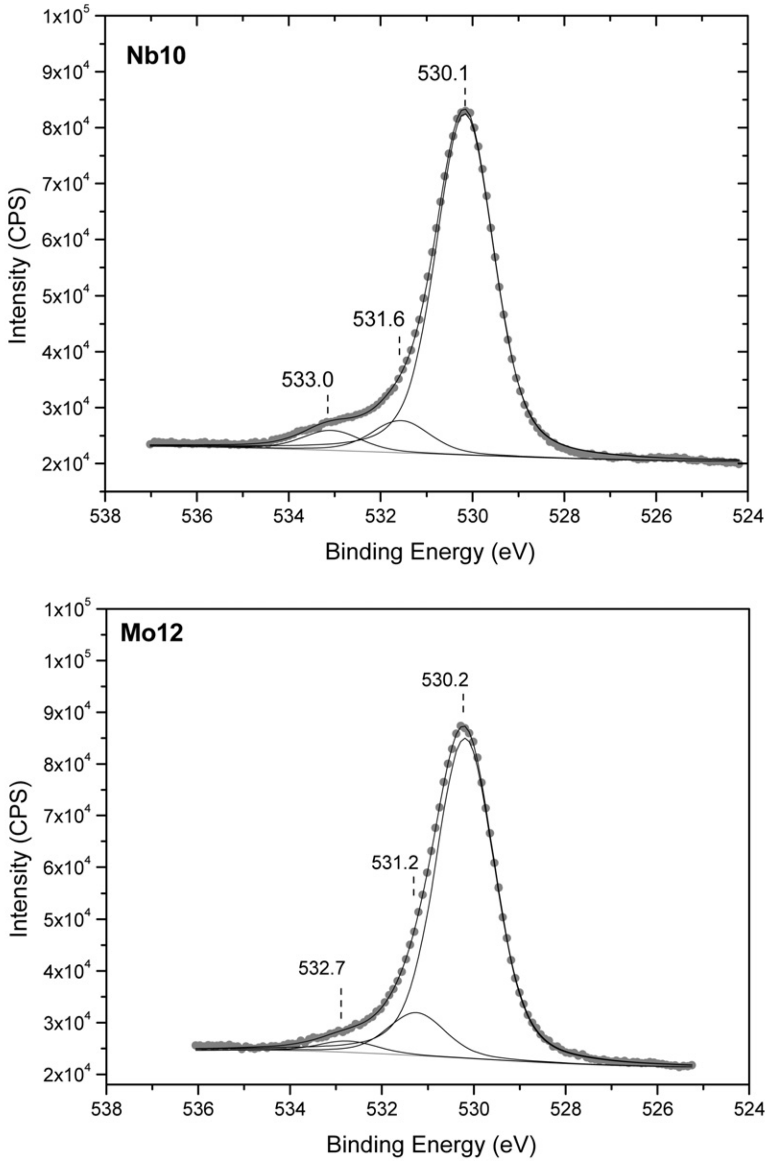

Fig. 4. XPS spectra corresponding to the O1s level for Nb10 and Mo12 samples. Dots: experimental points; full lines; fitting data.

Table 3
XPS data corresponding to the O1s level for Ti–M materials

Sample	O1s binding energy (eV)			Ti–OH (%)	M–OH (%)
	Ti–O	Ti–OH	M–OH		
V1.2	529.4	531.0	–	9.5	–
V5	529.5	530.9	–	11.9	–
V8	529.2	530.7	–	16.4	–
Mo8	530.1	531.3	532.7	9.0	2.9
Mo12	530.2	531.2	532.7	11.4	3.0
Mo26	530.3	531.3	532.2	5.6	3.7
Nb10	530.2	531.6	533.0	8.2	5.1
Nb20	530.1	531.7	533.2	9.7	6.0
W2	529.7	530.7	–	29.8	–
W11	530.1	532.1	–	5.8	–
W14	530.6	531.8	–	12.6	–
W26	530.6	531.6	–	13.9	–

third, weak contribution also was observed in Ti–Mo (Fig. 4) but it certainly was of much less importance than in the Ti–Nb case and possibly associated with Mo-rich zones of rather limited size [37,38] previously detected by Raman at the surface of the material. The relative intensities of the different oxygen species estimated using XPS are reported in Table 3.

UV–visible spectra of the Ti–Nb and Ti–Mo series are shown in Fig. 5, whereas those of the Ti–V and Ti–W series are presented in Fig. 3S in the Supplementary information. These plots enabled investigation of two main physicochemical features. First, unoccupied localized electronic states giving electronic transitions in the spectra were evident in the Ti–V case and, less significantly, in the Ti–Mo series and the Nb20 sample. Ti–V localized states have been previously analyzed with the help of UV–vis spectroscopy; Fig. 3S provides evidence of V(IV) d–d transitions around 550 nm and of V(V; vanadate) excitations around 450 nm [12]. Ti–Mo samples also displayed a broad band centered at ca. 550 nm containing contributions ascribable to Mo(V)–Mo(VI) intervalence charge transfer as well as Mo(V) d–d transition [39]. This band seemed to change its

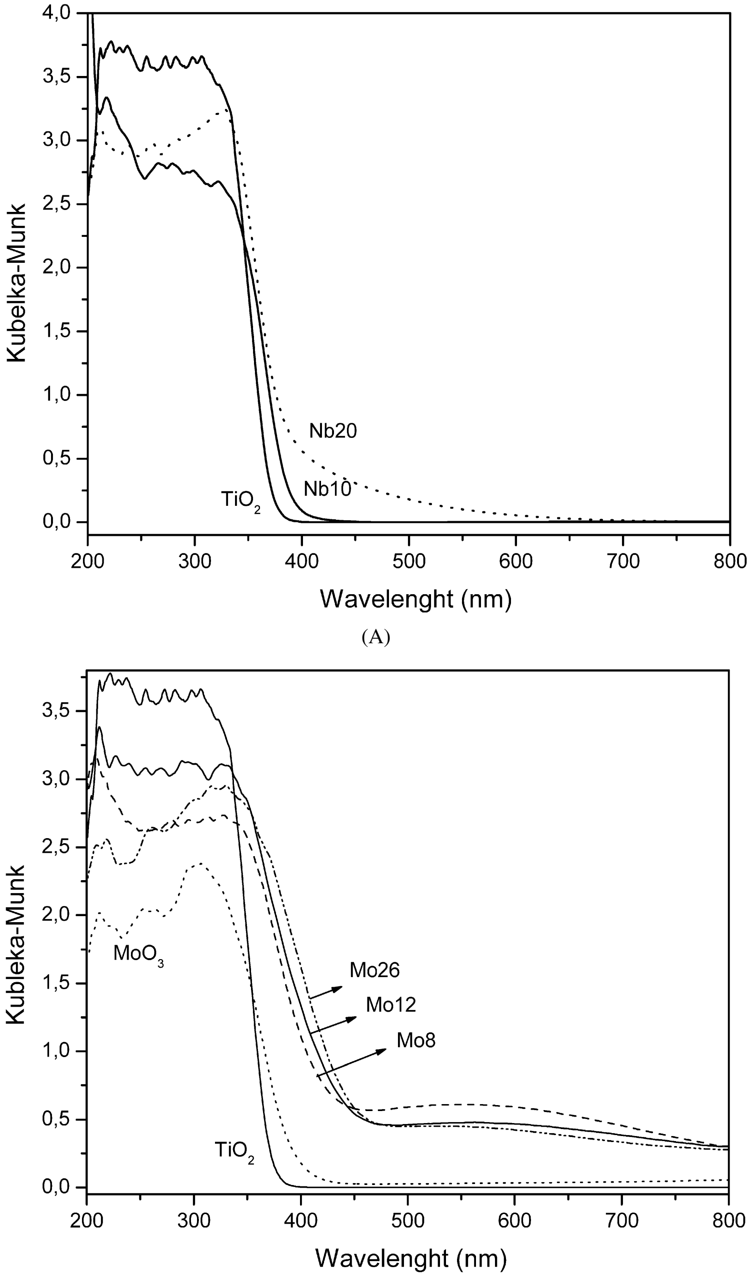

(A)

(B)

Fig. 5. UV–vis spectra of Ti–M samples and reference systems: (A) Ti–Nb, (B) Ti–Mo series of samples.

center with increasing Mo content, but this effect was of only moderate magnitude, in agreement with XPS results indicating a residual Mo(V) fraction. In the case of the Ti–Nb series, only the highest-loading sample displays an Urbach-type tail after the characteristic charge transfer band, which might be attributed to the presence of Nb-rich zones as discussed earlier. We analyze this further in the next section.

The second main feature extracted from the UV–visible study concerns the bandgap behavior as a function of the M heteroatom nature and concentration (Fig. 6). Whereas bulk TiO_2 is an indirect semiconductor, nanostructured materials can be direct semiconductors [40,41]. Bandgap values were estimated from the absorbance spectra using both types of analysis (i.e., for direct and indirect transitions); the trends observed were the same in both cases. Thus, Fig. 6 displays the calculated indirect bandgap energy. The value of ca. 3.1 eV obtained for nanostructured anatase-TiO_2 agrees well with previously reported data [6,40]. Trends depicted in this figure showed decreasing behaviors for all Ti–M systems. However, this decrease was somehow moderate (0.2 eV) for Ti–V, in accordance of the moderate concentration of V present into the TiO_2-anatase structure and reached a constant value after the solubility limit. It should be mentioned that the error in the bandgap estimation of Ti–V samples is large due to the presence of bands associated to localized states at ca. 450 nm, close to the bandgap [12]. Surprisingly, a small bandgap decrease was observed in the case of Ti–Nb,

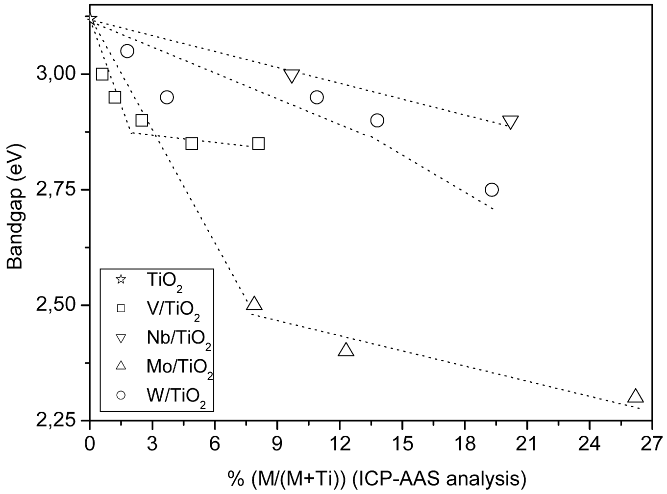

Fig. 6. Bandgap energy of the anatase phase of Ti–M materials as a function of the M atomic percentage. Dotted lines are only a guide for the aids.

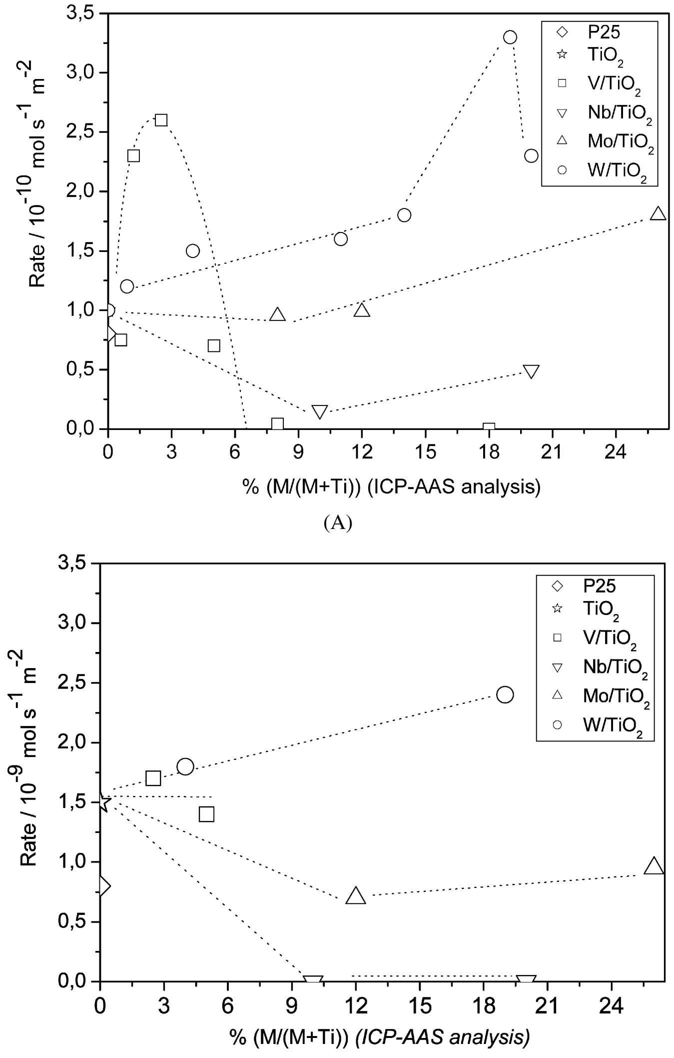

(A)

(B)

Fig. 7. Toluene photoelimination reaction rate displayed by Ti–M materials under: (A) sunlight, and (B) UV light excitations. Dotted lines are only a guide for the aids.

whereas more significant changes are detected for the Ti–Mo and Ti–W series.

Fig. 7 plots the activity of Ti–M samples in the photoelimination of toluene under sunlight (Fig. 7A) and UV (Fig. 7B) excitations. Fig. 4S in Supplementary information shows the time evolution of the reaction rate of the W19 photocatalyst throughout the experiment as a representative example of the behavior displayed by our samples. Only CO_2 (the major product responsible for ca. 75–95% of the selectivity) and benzaldehyde were detected as gas-phase products during reaction. Fig. 7 also includes data concerning the microemulsion-prepared TiO_2 reference and the (anatase + rutile) P25 (Degussa) material. Visual inspection of this figure gives evidence that the reaction rate displays three well-differentiated behaviors as a function of the M content of the Ti–M material. The V, Mo, Nb, and W single oxides displayed very low activity and thus are not included in this figure. For Ti–V, the figure shows a maximum located between 2.5 and 5 at% and practically null activity afterward. The Ti–Mo and Ti–W series display a two-linear behavior with a fist region, characteristic of low loading, with a different slope (Ti–W $\ll$ Ti–Mo). As can be seen in Fig. 7 and as has been reported elsewhere, Ti–W samples with a W content above the solubility limit showed a decrease in the reaction rate with respect to the W19 sample [21]. The third behavior takes into account the Ti–Nb system, which consistently demonstrated lower activity than the two single-oxide TiO_2/P25 reference systems. The overall maximum of photoactivity was obtained with the W19 sample, with an enhancement factor of 3.3/4.1 times with respect to the TiO_2/P25 references. Local maxima of the Ti–V and Ti–Mo series corresponded to the V2.5 and Mo26 samples, respectively, displaying enhancement factors of 2.3/2.7 and 1.8/2.2. The samples demonstrated stable reaction rates for about 10 h, but prolonged reaction tests are needed to study the long-term stability of these systems. The selectivity for toluene total oxidation (e.g., CO_2 product) was approximately constant in the Ti–Nb (ca. 75–80%), Ti–Mo (ca. 95%), and Ti–W (ca. 85%) cases and for Ti–V materials with a V content below or equal to 2.5 at% (ca. 95%), decreasing for samples with higher loadings (ca. 80%). Fig. 7B includes data obtained using UV light as excitation source. Experiments with selected samples showed that only for Ti–W was a slightly enhanced reaction ratio obtained, well below that obtained using sunlight excitation. Nonnegative (with respect to the TiO_2 reference) and essentially constant values were found for Ti–V, with negative (Ti–Mo) and rather negative (Ti–Nb) results observed in the remaining cases.

4. Discussion

Table 1 reports the main characteristics of the materials synthesized. As mentioned earlier, presence of the M heteroatom clearly affects morphological properties. The table demonstrates two general situations, in parallel to the structural situation of the M cation. When M occupies mainly anatase network positions (i.e., substitutional positions), in most cases an increased surface area and a concomitant and moderate decreased particle size with respect to the single TiO_2 oxide prepared by

Table 4
Main structural and electronic properties of the anatase-type phase of Ti–M materials

Doping metal	Tetra/vol.[a]	M local neighbor atom	Surface segregation (at%)[b]	Bulk/surface ox. state and coordination	Bandgap/mid-gap states[c]
V	−/−	Ti	–	$^{4+2}$V(IV)/^{5}V(V)	r.s./(−)
Nb	+/+	Nb, Ti	2.0	$^{4+2+1}$Nb(VI)/–	s.s./(+)
Mo	+/−	Ti, Mo	3.5	$^{4+2}$Mo(VI)/^{6}Mo(VI)[d]	r.s./(+)
W	−/−	Ti	2.5	$^{4+2}$W(VI)/^{5}W(VI)	r.s./(−)

[a] +, changes from TiO_2; −, absence of changes.

[b] Maximum M surface segregation for Ti–M samples below the M solubility limit of the anatase-type structure.

[c] r.s. = red shifted bandgap with respect to that of TiO_2 oxide; s.s. = small red shift. For Ti–V and Ti–Mo see text for further explanations.

[d] Mo(V) species detected below 5%.

microemulsion can be seen. A special case is Ti–V, in which low surface areas are observed. In this latter case, we can see a clear difference in surface area and primary particle size below/above 5 at%, indicating that the presence of surface V(V) may drive morphological variations, even when V(IV) is the dominant vanadium species of the Ti–V system. The presence of M atoms at the surface is in fact the second general situation in which we observe a decreased surface area for V8, V18, W20, W27, and Mo26. Thus, it may be suggested that our microemulsion-prepared Ti–M materials have a general tendency to display either an increasing surface area or decreasing particle size in the presence of group V/VI M elements at substitutional positions of the anatase structure, as well as a decrease in surface area when the M cation is at the surface of the material. It can be seen that minimal quantities of V(V) at the surface [even when V(IV) is the dominant chemical state] seem to produce the greatest effect on the morphological properties; although this property has been consistently reported, its underlying mechanism remains unknown [10–13].

The oxidation state of the M cations is rather defined and constant when in Ti–M mixed-metal oxide structures. The presence of V(IV) and Mo(VI) as the dominant (>95%) species and Nb(V), W(VI), and Ti(IV) as exclusive species is evident from the XPS results (Table 3). EPR data (not shown) and XPS allow us to dismiss the existence of Ti(III) species, whereas the absence of Raman bands characteristic of interstitial cations [31,32] and the XRD analysis demonstrate that M cations are dominantly occupying substitutional positions of the TiO_2-anatase structure up to the corresponding solubility limit. Considering this, the stoichiometry of the mixed oxide would be $Ti_{1-x}M_xO_{2+y}$ but with an O/(Ti + M) clearly dependent on the chemical nature of M. For V, this ratio is rather close to 2, whereas deviations from this value would be expected in the other three Ti–M series. Such deviations lead to the existence of defects related mainly to the M cation oxidation state and ionic radius. Whereas in the Ti–W case the dominant presence of cationic vacancies was demonstrated [22], more complex defects are expected in the Ti–Mo and Ti–Nb cases. In fact, the careful analysis of the Ti2p and O1s XPS peak, as detailed in Tables 2 and 3, provides significant information through the study of the M cation local order. Table 3 points out the absence of homo-atom (M–O–M) bonds in the first cation coordination shell of W in Ti–W, in agreement with the above-mentioned previous results [22], a certain small contribution of homo-atom bonds in Ti–Mo, and the increasing importance of M–O–M bonds for Ti–Nb. Thus, the presence of Mo- and Nb-rich zones within roughly homogeneous mixed oxides (Tables 2 and 3) is established.

The local environment around the M cation of the Ti–M mixed-metal substitutional solid solutions with anatase structure is summarized in Table 4. We stress that this table takes into account Ti–M samples below the corresponding solubility limit. The table highlights the differences among M local environments at bulk and surface positions extracted from our multi-technique XRD, Raman, and XPS approach. For bulk positions, a certain decrease in the local symmetry of the anatase cation positions is typically represented by a 4 + 2 coordination; this is clearly the case for V and W [12,22,42]. Mo approaches this situation somewhat when sited at anatase bulk positions, but Nb has a dominant local symmetry resembling that of the pure Nb_2O_5 oxide (4 + 2 + 1), although subjected to significant distortion originating from the structural constraints imposed by the anatase structure, as evidenced by the XPS binding energies reported in Tables 2 and 3. Concerning surfaces, Raman spectroscopy indicated the presence of penta-coordinated V and W species [with vanadium V(V) the dominant species at the surface] and of hexa-coordinated species for the Mo cations detected on the surface MoO_x patches [32]. Thus, in the case of Ti–V and Ti–Mo (>5 and 12 at%, respectively), we also detected M-rich zones characteristic of surface layers. However, Nb was depleted from the surface top layer (Fig. 3), although certainly not from the near-surface layers (Table 2; Fig. 4).

The marked differences in the bulk and surface local structures of the M cations mirror long-range order variations detected through Rietveld analysis of the anatase cell parameters (Fig. 1). To allow simple visual inspection of the structural distortions, Fig. 8 displays the tetragonality (a/c ratio) and cell volume for the Ti–M materials. Compared with the single TiO_2 oxide reference, introduction of the M cation can be seen to produce changes in cell parameters, which, however, lead to very moderate changes in tetragonality and cell volume for the Ti–V and Ti–W samples (with the exclusive presence of titania structures, e.g., <5 and 20 at%, respectively). This obviously reflects the presence of a well-defined local order around M and punctual defects of the anatase structure, derived from the minimal structural disturbance originated by the similar M^{n+} ionic

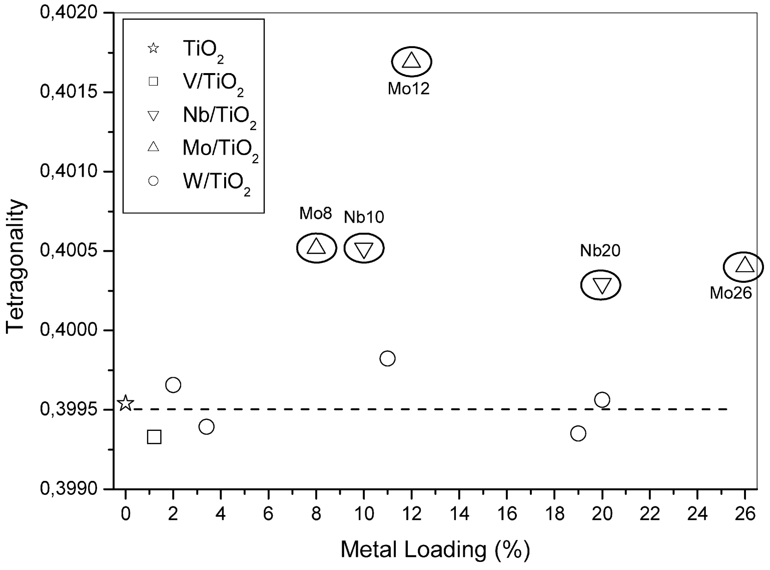

(A)

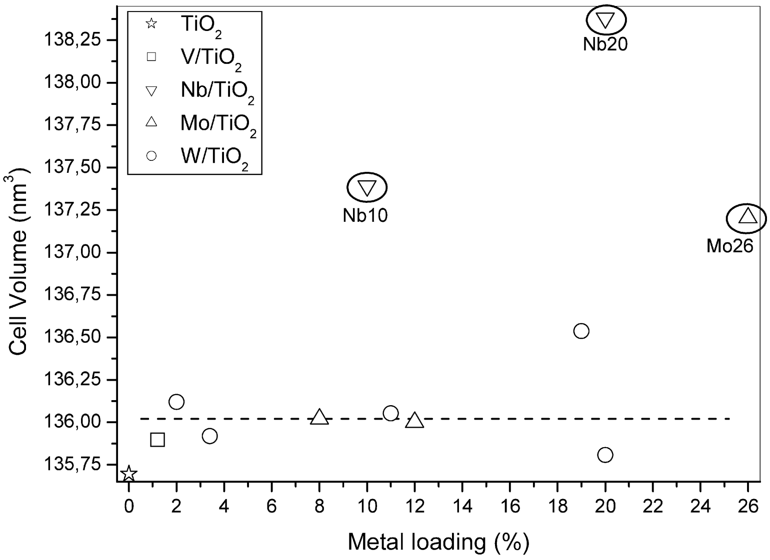

(B)

Fig. 8. (A) Tetragonality, and (B) cell volume of the anatase structure of Ti–M materials. Dashed lines are only a guide for the aids.

radii [V(IV), 0.58 nm; W(VI), 0.60 nm; Ti(IV), 0.605 nm [34]], and leading to minimum changes in tetragonality and cell volume (Table 4; Fig. 8). The reasonable ordering at long range also is evidenced by analyzing the main E_g Raman peak at ca. 144 cm^{-1} of the anatase-type structure on changing the M loading (Fig. 9). Simultaneous variations in peak position and width on oxide systems are related to several physicochemical effects, among which phonon confinement, structural defects, lattice contraction/expansion (position), and strain (width) are very important. Phonon confinement is a key contribution in nanostructured oxides [6]. The predicted effects of primary particle size (i.e., confinement effect) expected for a TiO_2 nanosystem are better visualized (due to resolution problems masking frequency variations) in the width [6]; for the pure TiO_2, these are depicted as a continuous line in Fig. 9. Comparison with the Ti–V and Ti–W samples highlights the fact that only W19 exhibits a strong additional effect on the width as a consequence of the presence of W.

In Ti–Mo, we detect a progressive departure from the anatase characteristics as a function of the M loading, leading to larger tetragonality values with respect to the parent TiO_2 reference oxide (Fig. 8) and greater expected width of the Raman E_g mode, taking into account confinement effects on TiO_2 (Fig. 9). The first finding indicates that Mo structural effects are crystallographically oriented and lead mainly to a shrinking of the d spacing normal to the anatase (001) face (c parameter), suggesting a strong interaction with this face. The higher surface energy of (001) relative to (100) [43] indicates that interaction with Mo is thermodynamically favored. A certain surface enrichment on anatase has been claimed for Y doping on this basis [44], in agreement with the presence of Mo as surface patches in the Ti–Mo samples, at least with Mo content above Mo12

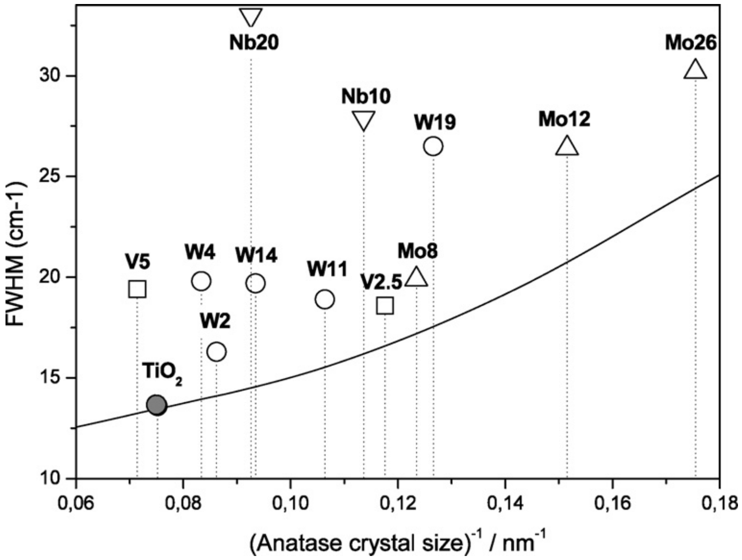

Fig. 9. Fwhm of the Raman E_g anatase-type band as a function of the inverse primary particle size. Theoretical expectations from the confinement model are shown as full lines. See text for further details.

(Figs. 2 and 3). However, this is a modest enrichment; overall, XPS does not show a strong surface enrichment on these materials, although it is greatest below the M–TiO_2 solubility limit (Table 4). For bulk positions, the lower Mo impact is suggested by the absence of differences in the cell volume (Fig. 8). The local enrichment due to preferential formation of M–O–M bonds progresses further when Nb is the heterocation. Both the XRD (Fig. 8) and Raman (Fig. 9) analyses show that the Nb-rich local ordering creates complex (e.g., extended) vacancy defects derived from the presence of Nb-rich zones, altering the tetragonality and cell volume of the anatase structure and yielding very large Raman line widths. As mentioned earlier, Nb is not in the surface top layer (Table 3) but seems to display a homogeneous radial profile (enrichment <2 at%), as deduced from Table 2.

As mentioned earlier, a summary of the short-range and long-range results obtained from the structural analysis of the Ti–M mixed-metal substitutional oxides (e.g., below the corresponding solubility limits) with anatase structure is presented in Table 4. In brief, our multitechnique approach indicates that the presence of V and W on such structures disturbs structural characteristics/properties only minimally, whereas increasing effects are seen for Mo and particularly for Nb. The four cations seem to present homogeneous radial profiles through the whole anatase nanoparticle with the exception of Ti–Mo samples, in which a modest Mo surface enrichment can be deduced from Table 2 before the neat detection of the Mo solubility limit at the anatase structure. A somewhat similar phenomenon occurs with V but can be detected only well above the solubility limit [12]. Concerning thus Ti–M samples below the corresponding M solubility limits, the appearance of local environments displaying MO_x local features is further reflected in the long-range order of the Ti–Mo and Ti–Nb nanostructured solids, as deduced from the tetragonally and/or cell volume variations (from the TiO_2 anatase-reference structure) summarized in Table 4. As discussed below, changes in the anatase cell parameters and characteristics have a critical influence on the electronic properties of the solids and thus on the charge recombination on light absorption, providing key information to explain the photochemical activity of the samples.

For our purposes, the electronic effects exerted by the presence of the M cations in substitutional positions of the TiO_2-anatase structure can be grouped mainly into two categories. The first concerns the creation of localized states in the TiO_2 gap, and the second implies variation of the bandgap energy by changes in either the valence or conduction bands. For our Ti–M samples, we found localized states in the case of V, Mo, and high loadings of Nb. V displayed V(IV) d–d transitions, whereas charge transfer levels of MoO_x/NbO_x entities were detected in the corresponding UV–visible spectra. In Ti–V, our results under UV light (Fig. 7B) as well as previous findings [45] showed that the V(IV) d–d localized transitions do not negatively affect charge recombination. In contrast, a clear correspondence between the presence of the other type of localized states and charge recombination can be deduced from results obtained under UV illumination (Fig. 7B). This figure shows that the presence of Nb and Mo is always detrimental for TiO_2 activity; because surface (e.g., presence of Nb at the surface) and significant confinement-size effects (Table 1) on photoactivity are clearly out of Ti–Nb, this is a strong indication of a detrimental recombination effect, as was postulated previously [19]. Thus, we can establish a direct link between the presence of MO_x entities (irrespective of the presence of MoO_x clusters at the surface or NbO_x entities at the bulk) and an adverse effect on photochemical activity under sunlight excitation. Table 3 suggests a stronger effect in parallel to the increasing number of MO_x clustering entities present in M-rich local zones. This also occurs in the Ti–V system in the presence of VO_x species (e.g., above the V solubility limit at the anatase structure); as discussed earlier, the presence of V(V) is detrimental for photoactivity [12]. We can again establish that interband charge transfer V(V)O_x-associated mid-gap states progressively enhance charge recombination as the V content of the material increases over the V anatase solubility limit. The second electronic effect is derived from the bandgap red shift promoted by the presence of the M cations on the anatase structure. This is illustrated in Fig. 6. We can see that a roughly linear decrease occurred for the four cations in the range of substitutional solid solution formation, as expected from theoretical basis. However, we found an initial slope in the order Ti–Nb < Ti–W < Ti–Mo < Ti–V.

These two main electronic effects—presence of localized mid-gap states and variation of the bandgap energy—produced on M doping of the anatase structure are summarized in Table 4. The combination of the two main electronic effects allows straightforward rationalization of the photochemical activity displayed in Fig. 7A. Whereas enhancement of the visible light absorption power would drive the activity in the order Ti–Nb < Ti–W < Ti–Mo < Ti–V, Ti–Mo and particularly Ti–Nb series have a strong drawback derived from the homocation-enriched local order (around M cations), which generates "localized" electronic states and enhances charge recombination. In contrast, the main drawback of Ti–V is derived from its relatively low solubility limit, although the series displays the minimum structural disturbance of the anatase structure through the absence of charge-neutrality-derived defects. This leaves the Ti–W series as the one among our systems with the optimum potential. In this case, we detected a positive influence of W under both sunlight (Fig. 7A) and UV light (Fig. 7B), with the first clearly superior, indicating the prevalence of the visible light contribution under sunlight excitation. Note that other potential influences in photochemical activity coming from changes in surface adsorption of the hydrocarbon and/or oxygen were analyzed using infrared and EPR and were founded with no direct relationship with chemical activity, as reported previously in some of the series [21,22,46,47].

Thus, a structure–electronic connection can be established based on the multitechnique study of the solids. It can be seen that the presence of local ordering (MO_x "single-oxide" clustering) on Ti–M anatase-type substitutional mixed oxides, irrespective of its presence at surface or bulk positions, originates localized (i.e., charge transfer type within MO_x cluster entities) electronic states involved directly in charge recombination and thus has a detrimental effect on photoactivity. Our findings indicate that the production of Ti–M anatase-type mixed oxides with minimal structural disturbance is a viable way to obtain highly active visible light-driven photocatalysts. Toward this end, we should point out that, based on the present results, further enhancement of the photochemical activity in organic pollutant elimination of Ti–M substitutional mixed oxides with anatase structure can be envisaged. First, we may speculate that careful control of the solution chemistry of aqueous multication Mo (and, less importantly, Nb) entities present in the initial step of the microemulsion procedure may facilitate the consecution of more homogeneous Ti–Mo samples and significantly reduce or ultimately eliminate the adverse enhancement of charge recombination originated from the presence of MoO_x entities. A second pathway involves the combination of V with high-solubility doping cations like W and Mo. Both of these pathways are currently under study.

5. Conclusion

The present work has explored the synthesis of Ti–M (M = V, Nb, Mo, W) mixed-metal oxides with anatase-type structure. Samples containing M cations up to ca. 2.5 (V) or 20 (Nb, Mo, W) at% in substitutional positions of the anatase network were obtained. The presence of V and W in such structures was found to minimally disturb local/long-range structural characteristics of the TiO_2-anatase phase, with increasing effects detected for Mo and particularly Nb. The appearance of MO_x local environments in the latter two cases (irrespective of their dominant presence at bulk or surface positions) yielded "localized" electronic states that are believed to be directly implied in enhancing charge recombination with respect to the bare TiO_2 single oxide prepared in similar conditions.

The four M cations inserted in the TiO_2-anatase structure produce a red shift of the anatase bandgap, enhancing the visible light absorption power in the following order: Ti–Nb < Ti–W < Ti–Mo < Ti–V. The trade-off between this positive effect and those mentioned earlier involved in charge recombination indicates that a significant enhancement of photochemical activity is possible only under our preparation conditions for Ti–V and Ti–W. The activity data suggest that Ti–V is the optimum choice (i.e., it displays higher activity for the same M loading), but the activity enhancement is limited thermodynamically by the low solubility limit of the heterocation on the anatase structure. These results imply that maximization of photoactivity was obtained within the Ti–W series.

Acknowledgments

A.K. thanks the CSIC for an I3P postdoctoral grant. Financial support was provided by projects CTQ2004-03409/BQU, CTQ2004-05734-CO2-02, CTQ-2007-60480/BQU, and P06-FQM-1406.

Supporting information

Supplementary material for this article may be found on Science Direct, in the online version.

Please visit doi: 10.1016/j.jcat.2008.01.005.

References

[1] H. Bosh, F. Janssen, Catal. Today 2 (1988) 369.

[2] P. Forzatti, Catal. Today 62 (2000) 51.

[3] M.R. Hoffman, S.T. Martin, W. Choi, D.W. Bahneman, Chem. Rev. 95 (1995) 69.

[4] H.B. Thu, M. Karkmaz, E. Puzenat, C. Guillard, J.M. Herrmann, Res. Chem. Intermediat. 31 (2005) 449.

[5] A. Maldoti, A. Molinari, R. Amadeni, Chem. Rev. 102 (2002) 3811.

[6] M. Fernández-García, A. Martínez-Arias, J.C. Hanson, J.A. Rodriguez, Chem. Rev. 104 (2004) 4063.

[7] M.M. Cohen, Introduction to the Theory of Semiconductors, Gordon, Amsterdam, 1999.

[8] N.I. Al-Salim, S.A. Bagshaw, A. Bittar, T. Kemmit, A.J. McQuillan, A.M. Mills, M.J. Ryan, J. Mater. Chem. 10 (2000) 2358.

[9] V. Luca, S. Thomson, R.F. Howe, J. Chem. Soc. Faraday Trans. 93 (1997) 2195.

[10] M. Anpo, M. Takeuchi, J. Catal. 216 (2003) 505.

[11] J.J. Shyre, M.R. DeGrure, J. Am. Chem. Soc. 127 (2005) 12736.

[12] A. Kubacka, A. Fuerte, A. Martínez-Arias, M. Fernández-García, Appl. Catal. B 74 (2007) 26.

[13] L.E. Depero, L. Sagaletti, B. Allieri, E.L.E. Bontempi, A. Marino, M. Zachii, J. Cryst. Growth 198 (1999) 516.

[14] J.A. Wang, R. Limas-Ballesteros, T. López, A. Moreno, R. Gómez, O. Novaro, X. Bokhim, J. Phys. Chem. B 105 (2001) 9692.

[15] C. Adán, A. Bahamonde-Santos, M. Fernández-García, A. Martínez-Arias, Appl. Catal. B 72 (2007) 11.

[16] J.C. Yu, J. Lin, R.W.M. Kwok, J. Phys. Chem. B 102 (1998) 5094.

[17] M.D. Hernández-Alonso, J.M. Coronado, B. Bachiller-Baeza, M. Fernández-García, J. Soria, Chem. Mater. 19 (2007) 4283.

[18] V. Guidi, M.C. Carotta, M. Ferroni, G. Martinelli, M. Sacerdoti, J. Phys. Chem. B 107 (2003) 120.

[19] A. Mattson, M. Leideburg, K. Larsson, G. Westin, L. Osterlund, J. Phys. Chem. B 110 (2006) 1210.

[20] M.S. Jeon, W.S. Yoon, H. Joo, T.K. Lee, H. Lee, Appl. Surf. Sci. 165 (2000) 209.

[21] A. Fuerte, M.D. Hernández-Alonso, A.J. Maira, A. Martínez-Arias, M. Fernández-García, J.C. Conesa, J. Soria, G. Munuera, J. Catal. 212 (2002) 1.

[22] M. Fernández-García, A. Martínez-Arias, A. Fuerte, J.C. Conesa, J. Phys. Chem. B 109 (2005) 6075.

[23] X.C. Dai, H.Y. Xiao, W.S. Li, Y.Q. Na, Appl. Catal. A 290 (2005) 25.

[24] F.R. Sensato, R. Custodio, E. Longo, A. Beltrán, J. Andrés, Catal. Today 85 (2003) 145.

[25] F. Fresno, D. Tudela, J.M. Coronado, M. Fernández-García, A. Hungría, J. Soria, Phys. Chem. Chem. Phys. 8 (2006) 2421.

[26] G.K. Willianson, W.H. May, Acta Metall. 1 (1953) 22.

[27] A.J. Maira, K.L. Yeung, J. Soria, J.M. Coronado, C. Belver, C.Y. Lee, V. Augugliaro, Appl. Catal. B 29 (2001) 327.

[28] G. Busca, G. Ramis, J.M.G. Amores, V.S. Escribano, P. Piaggio, J. Chem. Soc. Farady Trans. 90 (1994) 3181.

[29] M. Mikami, S. Nakamura, O. Kitao, H. Arakawa, Phys. Rev. B 66 (2002) 155213.

[30] R.L. Frost, K.L. Erickson, M.L. Weier, O. Carmody, Spectrosc. Acta A 61 (2005) 829.

[31] F.D. Hardcastle, I.E. Wachs, J. Raman Spectrosc. 26 (1995) 397.

[32] Y. Chen, I.E. Wachs, J. Catal. 217 (2003) 468.

[33] C.D. Wagner, W.M. Riggs, L.E. Davis, J.F. Moulder, Handbook of X-Ray Photoemission Spectra, G.E. Muilenber (Ed.), Perkin–Elmer, Minnesota, 1976.

[34] R.D. Shanon, Acta Crystallogr. A 32 (1976) 751.

[35] G. Colón, M.C. Hidalgo, G. Munuera, I. Ferino, M.G. Cutrufello, J.A. Navío, Appl. Catal. B 63 (2006) 45.

[36] R. Wojcieszak, A. Jasik, S. Monteverde, M. Ziolek, M.M. Vetar, J. Mol. Catal. A Chem. 256 (2006) 225.

[37] A. Katrib, A. Benadda, U.W. Sobczak, G. Maire, Appl. Catal. A 242 (2003) 31.

[38] C.V. Ramana, V.V. Atuchin, V.G. Kesler, V.A. Kochubey, L.D. Pokrovsky, V. Shutthanadan, U. Becker, R.C. Ewing, Appl. Surf. Sci. 253 (2007) 5368.

[39] M. Dieterle, G. Weinberg, G. Mesta, Phys. Chem. Chem. Phys. 4 (2002) 812.

[40] N. Serpone, D. Lawless, V. Khairutdinov, J. Phys. Chem. 98 (1995) 16646.

[41] K.M. Reddy, S.V. Mamorama, A.M. Reddy, Mater. Chem. Phys. 78 (2002) 239.

[42] T. Umebayashi, T. Yamaki, H. Itoh, K. Asai, J. Chem. Phys. Solids 63 (2002) 1909.

[43] M. Lazzeri, Phys. Rev. B 63 (2001) 155409.

[44] B. Chen, H. Zhang, B. Gilbert, J.F. Banfield, Phys. Rev. Lett. 98 (2007) 106103.

[45] X.-G. Hou, F.-X. Hao, B. Fan, X.-N. Gu, X.-Y. Wu, A.-D. Liu, Nucl. Instrum. Methods Phys. Res. B 243 (2006) 99.

[46] A. Fuerte, M.D. Hernández-Alonso, A.J. Maira, A. Martínez-Arias, M. Fernández-García, J.C. Conesa, J. Soria, Chem. Commun. (2001) 2178.

[47] A. Fuerte, M.D. Hernández-Alonso, A. Martínez-Arias, J.C. Conesa, J. Soria, M. Fernández-García, Phys. Chem. Chem. Phys. 5 (2003) 2913.